Journal of Materials Chemistry A

ROYAL SOCIETY OF CHEMISTRY

PAPER

View Article Online
View Journal | View Issue

Cite this: J. Mater. Chem. A, 2023, 11, 15821

Atomistic design of two-dimensional covalent organic frameworks with high thermoelectric performance†

Tingxia Zhou, [a] Xiaomei Wu,[a] Tianqi Deng, [bc] Haoyuan Li, [d] Zhibin Gao [e] and Wen Shi*[a]

Received 10th April 2023
Accepted 26th June 2023

DOI: 10.1039/d3ta02146g

rsc.li/materials-a

Very recently, burgeoning two-dimensional covalent organic framework-based materials have been proven to exhibit decent performance for potential thermoelectric applications. Nevertheless, hitherto formulating systematic atomistic-level materials design strategies for two-dimensional covalent organic frameworks with enhanced thermoelectric performance still remains a formidable challenge. Here, on the basis of *ab initio* computations, and taking 17 representative two-dimensional covalent organic frameworks as examples, an atomistic understanding is established to uncover the complex correlation among the macroscopic thermoelectric properties, nontrivial transport processes, and basic chemical structures, and concurrently, general materials design guidelines are offered. We reveal that the ratio of contributions of linker and knot parts to the valence bands can be treated as a strong predictor to assess the thermoelectric performance of covalent organic frameworks. Our results corroborate that a small ratio of the contributions of the linker and knot parts to the valence bands brings about a large band dispersion, weak interactions of charge carriers with lattice vibrations, high hole mobility, and thus an outstanding thermoelectric power factor. Furthermore, our findings reveal that for two-dimensional covalent organic frameworks, introducing benzene rings, replacing the heterocycles with benzene rings, reducing the number of nitrogen heterocycles, and avoiding benzoquinone structures in the linker parts help in realizing their charge-carrier delocalization, and thus a decent power factor.

Introduction

Thermoelectric (TE) materials offer an environment-friendly energy solution for direct heat-electricity interconversion. Systematic development of high-performance TE materials lies at the heart of modern thermoelectrics.[1] The performance of a TE material is determined using a dimensionless figure of merit, $zT = S^2\sigma T/k$, where $S^2\sigma$ is the power factor; S is the Seebeck coefficient; σ is the conductivity; k is the total thermal conductivity, and T is the temperature.[2,3] In general, a high-efficient TE material simultaneously calls for a large Seebeck coefficient and superb conductivity, but a poor thermal conductivity. Nevertheless, hitherto rational design of high-performance TE materials still remains an exacting challenge, due to the mutually restrictive relationships among TE transport parameters.[4] For instance, along with the enhancement of conductivity, the Seebeck coefficient dramatically attenuates, and the electronic thermal conductivity increases.

Due to their fascinating advantages, such as inexpensiveness, low toxicity, ease of manufacture, and inherently low thermal conductivity, innovative organic-based TE materials have attracted extensive research interest recently,[5,6] and nowadays, π-conjugated polymeric TE materials can show a figure of merit comparable to that of state-of-the-art inorganic ones at room temperature,[7–9] ensuring their potential commercial applications. Unlike conventional polymers, burgeoning covalent organic frameworks (COFs) are a class of crystalline polymers with highly ordered structures, which endows them with structural controllability and predesignability.[10–13] Importantly, their diversity of organic units, covalent linkage, and topological structure enables them to exhibit manageable and versatile functions, such as optoelectronics,[14] photovoltaics,[15] and thermoelectrics.[16]

Very recently, a series of impressive experimental advances have demonstrated that COFs are capable of exhibiting decent performance for TE applications,[17,18] and their unique

[a]School of Chemistry, Sun Yat-sen University, Guangzhou, 510006, China. E-mail: shiw59@mail.sysu.edu.cn

[b]State Key Laboratory of Silicon Materials, School of Materials Science and Engineering, Zhejiang University, Hangzhou, Zhejiang, 310027, China

[c]Institute of Advanced Semiconductors, Zhejiang Provincial Key Laboratory of Power Semiconductor Materials and Devices, ZJU-Hangzhou Global Scientific and Technological Innovation Center, Zhejiang University, Hangzhou 311215, China

[d]School of Microelectronics, Shanghai University, Shanghai, 201800, China

[e]State Key Laboratory for Mechanical Behavior of Materials, Xi'an Jiaotong University, Xi'an, Shaanxi, 710049, China

† Electronic supplementary information (ESI) available. See DOI: https://doi.org/10.1039/d3ta02146g

structural features may provide potentially paradigm-changing mechanisms to design new materials with outstanding performance.[19] For example, it is proven that a fluorene-based two-dimensional COF possesses a high Seebeck coefficient of 2450 μV K^{-1} and power factor of 0.063 μW m^{-1} K^{-2} at room temperature.[17] Furthermore, a new covalently bonded pyrene based fully fused aromatic π-conjugated two-dimensional organic network is reported to show an extremely high hole mobility of 501 cm^2 V^{-1} s^{-1} and conductivity of 1038 S cm^{-1} at room temperature.[18] These significant experimental achievements corroborate that emerging COFs offer a promising platform for heat-electricity interconversion functional materials.

It is worth noting that a prerequisite for further enhancement of materials performance and rational discovery of new ones is not only advancing the understanding of the microscopic TE transport processes determining the performance, but also establishing straightforward structure–function relationships. However, previous experimental studies on the TE properties of COFs mostly focused on materials preparation and performance measurement, and for this emerging class of materials, owing to the lack of fundamental investigations, their nonintuitive TE transport unfortunately remains poorly understood to date, unavoidably impeding systematic materials design.

To deal with the aforementioned critical problems, we herein take 17 representative two-dimensional COFs with fused ring structures as examples to conduct comprehensive *ab initio* computational explorations on their p-type TE properties by utilizing density functional theory (DFT), Boltzmann transport equation, and deformation potential (DP) theory. We establish an atomistic-level picture to unveil the complex interplay between the macroscopic TE performance, nontrivial transport processes, and basic chemical structures of COFs. Concurrently, general materials design guidelines for COFs with enhanced TE response performance are provided.

Computational methods

Model setup and structural optimizations

For our studied 17 two-dimensional COFs, we focus on their intralayer p-type TE properties, and monolayer structural models were built. The single-layer two-dimensional COFs lie in the *ab* plane, and to avoid the interlayer interactions, the unit cell lengths along the *c* axis were fixed at 20 Å. Both the lattice constants (*i.e.*, *a* and *b*) and atomic positions were optimized by using the projector augmented-wave (PAW) method[20] with the Perdew–Burke–Ernzerhof (PBE) exchange–correlation functional[21] including Grimme's D3 dispersion correction[22] in the Vienna *Ab initio* Simulation Package (VASP)[23] (version 6.2.1). The *Γ* *k*-points of 4 × 4 × 1 and 2 × 2 × 1 were used during the structural optimizations. The cutoff energy for the plane-wave basis set was 500 eV. The convergence criterion for the total energy was set to be 10^{-5} eV, and the residual force on each atom should be smaller than 0.01 eV $Å^{-1}$. The *Γ* *k*-points of 6 × 6 × 1 and 4 × 4 × 1 were used for single-point energy and charge density calculations. The details for model setup and geometric optimizations can be found in Section 1 of the ESI.†

Electronic structure characterization

Electronic structure calculations were carried out by the PAW method[20] with the PBE functional[21] including Grimme's D3 dispersion correction[22] in the VASP.[23] The cutoff energy was set to be 600 eV. The convergence criterion for the total energy was set to be 10^{-6} eV. The projected band structures were obtained by projecting the Kohn–Sham wave functions onto the spherical harmonic centered at the position of the ions based on the formula, $P_{Nlmn\boldsymbol{k}} = Y_{lm}{}^{N}|\phi_{n\boldsymbol{k}}$.[24] Here, $Y_{lm}{}^{N}$ is the spherical harmonic centered at ion index *N* with angular moment *l* and magnetic quantum number *m*; $\phi_{n\boldsymbol{k}}$ is the Kohn–Sham wave function with band index *n* and wave vector $\boldsymbol{k}$. In addition, the electronic structures of isolated knot and linker parts were computed by using the B3LYP (Becke, 3-parameter, Lee–Yang–Parr) functional[25] and 6-31+G(d) basis set in the Gaussian 09 program[26] (version A.02).

Boltzmann transport equation for TE performance calculations

We employed the Boltzmann transport equation[27,28] to evaluate the TE transport coefficients, including the conductivity (σ), Seebeck coefficient (S), power factor ($S^2\sigma$), and mobility (μ):

$$\sigma = \frac{2e^2}{\Omega}\sum_k \left[-\frac{\partial f_0(\varepsilon_k)}{\partial \varepsilon_k}\right] v_k v_k \tau_k, \tag{1}$$

$$S = \frac{2}{\Omega}\frac{e}{\sigma T}\sum_k v_k v_k \tau_k \left[-\frac{\partial f_0(\varepsilon_k)}{\partial \varepsilon_k}\right](\varepsilon_k - \varepsilon_F) \tag{2}$$

$$\mu = \frac{\sigma}{eN}. \tag{3}$$

Here, e is the elementary charge; Ω is the unit cell volume; $f_0(\varepsilon_k) = 1/\{\exp[(\varepsilon_k - \varepsilon_F)/k_B T] + 1\}$ is the Fermi–Dirac distribution function; ε_k is the band energy at a given k point; ε_F is the Fermi energy; k_B is the Boltzmann constant; T is the temperature; $v_k = \nabla_k \varepsilon_k/\hbar$ is the group velocity, which can be attained from the band structure calculations; $\hbar$ is the reduced Planck's constant; τ_k is the relaxation time; and $N = 2/\Omega\sum_k[1 - f_0(\varepsilon_k)]$ is the hole concentration. The dense Monkhorst–Pack k meshes of 35 × 35 × 2 and 39 × 39 × 2 were used to calculate the TE transport coefficients by summation in the k-space.[29]

Scattering time calculations

According to Fermi's golden rule, the relaxation time (τ_k) can be expressed as:

$$\frac{1}{\tau_k} = \frac{2\pi}{\hbar}\sum_{k'}\left|M\left(\boldsymbol{k},\boldsymbol{k}'\right)\right|^2 \delta\left(\varepsilon_k - \varepsilon_{k'}\right)(1 - \cos\theta) \tag{4}$$

where $|M(\boldsymbol{k},\boldsymbol{k}')|^2$ is the scattering matrix element; $\delta(\varepsilon_k - \varepsilon_{k'})$ is the Dirac δ function ensuring energy conservation in the charge carrier scattering process; and θ is the scattering angle.

DP theory for lattice vibration scattering

On the basis of the DP theory,[30], $|M(\boldsymbol{k},\boldsymbol{k}')|^2$ can be expressed as

$$\left|M\left(\boldsymbol{k},\boldsymbol{k}'\right)\right|^2 = \frac{k_B T E_1^{\,2}}{\Omega C_{ii}} \quad (5)$$

where E_1 is the DP constant and C_{ii} is the elastic constant. Both of them can be obtained from first-principles computations.[31–34] The elastic constant was evaluated by stretching the unit cell along the crystal axis a, b, and c directions separately by ±0.5% and ± 1.0%, and then fitting the total energy (E) of the deformed lattice ($\Delta l/l_0$) *via* the equation, $(E - E_0)/\Omega = [C_{ii}(\Delta l/l_0)^2]/2$, where E_0 and l_0 are the total energy and lattice parameter at equilibrium, respectively, and Δl is the change of lattice parameters. To attain the DP constant, we calculated the band energies with the lattice deformation and then fitted the valence band maximum to the dilation ($\Delta l/l_0$) *via* the equation, $E_1 = \Delta E_{VBM}/(\Delta l/l_0)$, where ΔE_{VBM} is the absolute position change of the valence band maximum with the lattice deformation. The vacuum energy level calibration method[35,36] was utilized to calculate the absolute energy level of the valence band maximum. The related computational details and schematic diagram of the vacuum energy calibration method are displayed in Section 1 of the ESI.†

Results and discussion

Geometric structure of two-dimensional COFs

Two-dimensional COFs consist of knot and linker units, and their chemical structures dictate the shape and size of COFs. Consequently, by engineering and matching the geometric structures of building blocks in COFs, their skeleton structures can be rationally tailored. In experiments, a variety of two-dimensional COFs with fused ring linkages have been reported in recent years.[18,37–41] On the basis of these advances, it can be seen that fused ring structures highly restrict the free torsion of the backbone, naturally resulting in a rigid conformation and thereby remarkable thermal and chemical stabilities.[37,42] In addition, such a class of two-dimensional COFs can endow them with delocalized π orbitals, benefiting from excellent intrachain charge transport properties.[38,39] Consequently, we focus on two-dimensional COFs with fused ring structures. Here, we take 17 typical two-dimensional COFs as examples to explore their p-type TE properties, and they all exhibit hexagonal topological diagrams (Fig. 1 and S6†). On the whole, from the standpoint of topological structures of our studied systems, their knot parts can be regarded as benzene rings, and their linker parts are different (Fig. 1 and S6†).

Specifically, Fig. 1 and S6† show that the linker units of **1** and **2** are the benzene and three fused benzene rings, respectively. **3–9** possess the linker parts of nitrogen heterocycles. The linker units of **10–13** contain heterocycles with the oxygen group elements (*i.e.*, O, S, and Se). **14** and **15** have the linker parts of nitrogen heterocycles and benzoquinone. Moreover, **16** and **17** possess the linker fragments of nitrogen and oxygen heterocycles.

Density-functional computations are conducted to probe the Ångström-level structural feature for our studied two-dimensional COFs, and our results of geometric optimizations reveal that the diversity of their linker units brings about the difference in the in-plane lattice parameters (Table S2†). As an example, for **1**, **4**, **10**, **12**, and **13** with the linker parts of one six-membered ring, their lattice parameters fall in the range of 8.25–9.71 Å, and for **2–3**, **5–9**, **11**, and **14–17** with the linker units of three six-membered rings, their lattice constants are around 16.2–17.2 Å (Table S2†). Therefore, we speculate that for our studied systems, their geometric diversity can give rise to multiple electronic structure properties.

Descriptions of electronic structures

Usually, two-dimensional monolayer COFs can be treated as an extension into a second dimension of the one-dimensional polymer chain. Previous theoretical studies have demonstrated that π-conjugated polymer chains can exhibit dispersive band structures and thereby decent charge transport properties.[32,34,43–45] To investigate the electronic properties of

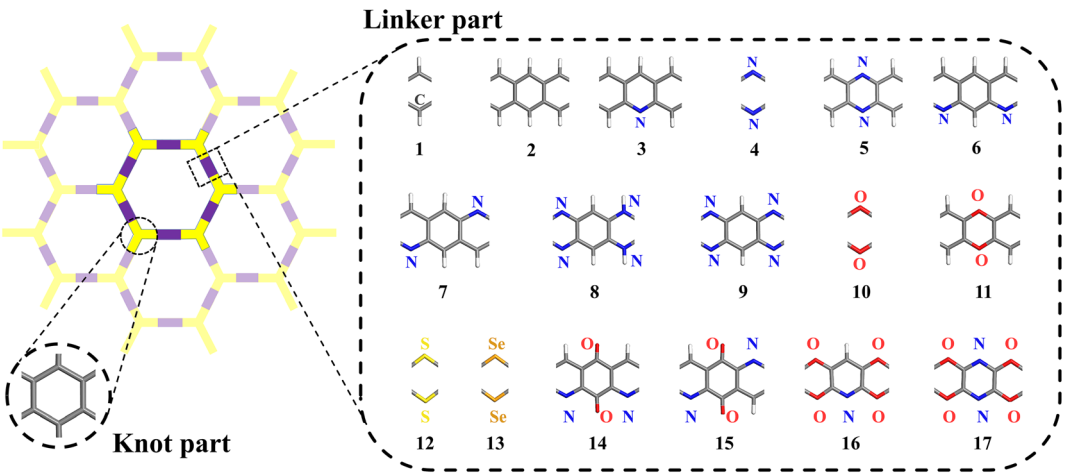

Fig. 1 Topological diagrams and chemical structures of our studied 17 two-dimensional COFs with fused ring structures. The carbon, nitrogen, oxygen, sulphur, selenium, and hydrogen atoms are represented in grey, blue, red, yellow, orange, and white, respectively. The schematic diagram of the model setup is displayed in Fig. S1.† Their optimized lattice parameters are shown in Fig. S2 and Table S2.†

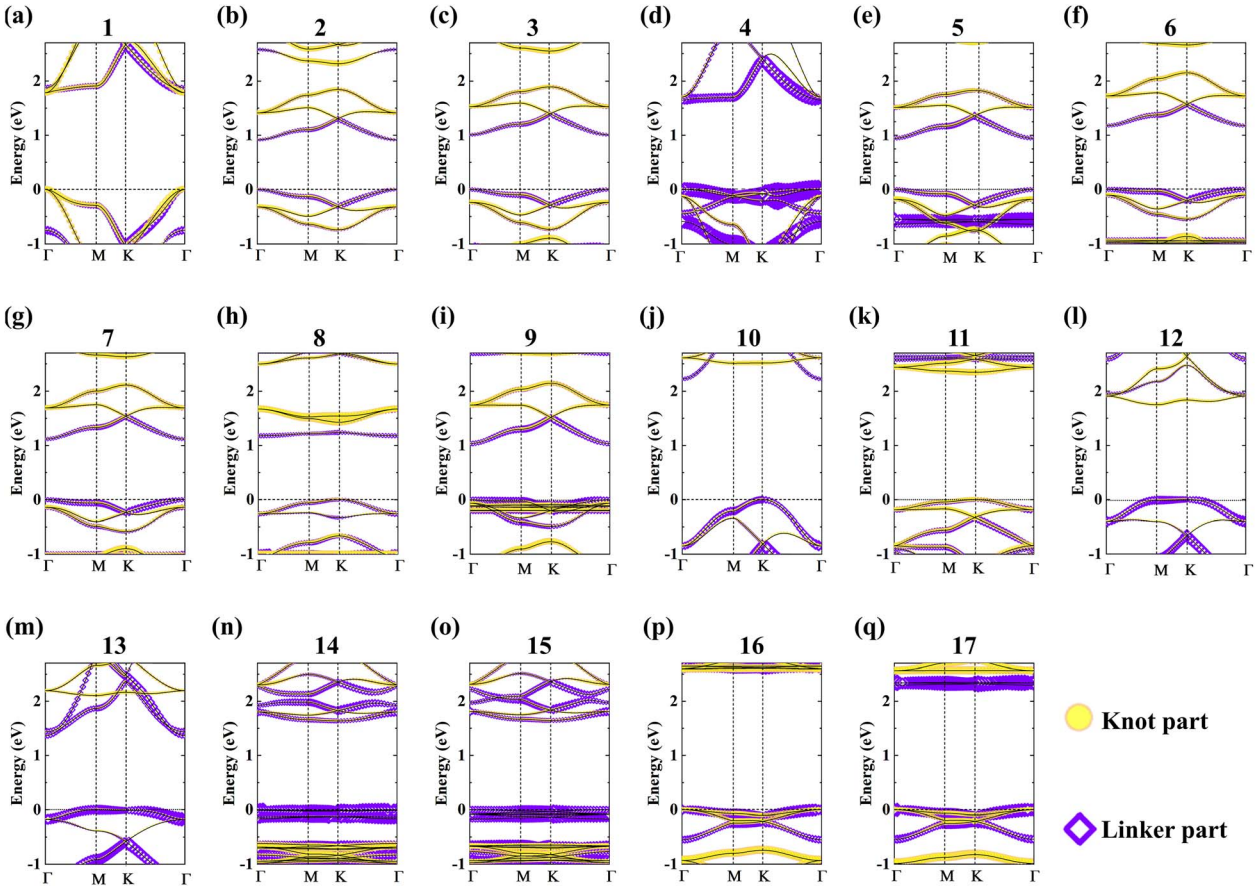

Fig. 2 Contribution of knot (yellow circle) and linker (violet diamond) parts to the band structures of our studied 17 two-dimensional COFs. The symbol size denotes the relative weight of the component ratio. The non-projected band structures are shown in black solid lines. The Fermi energy levels are displayed in black horizontal dashed lines. The reciprocal coordinates of high symmetry k-points in the first Brillouin zone are Γ = (0, 0, 0), M = (1/2, 0, 0), and K = (1/3, 1/3, 0). The quantified contributions of the knot and linker parts to the valence band are summarized in Table S3.† The element projected band structures are shown in Fig. S7.† The quantified contributions of different elements to the valence band are listed in Table S4.†

our studied materials, the descriptions of their band structures are offered. Fig. 2 and Table S3† show their projected band structures of knot and linker parts, and obviously, all these two-dimensional COFs exhibit typical semiconductive characteristics with bandgaps in the range of 0.917–2.59 eV. Additionally, it is found that valence band dispersions vary widely for our studied systems (Fig. 2 and Table S3†). For instance, **1** possesses the largest valence band dispersion of 1.05×10^3 meV, yet **14** shows the smallest one of 25.0 meV (Fig. 2 and Table S3†). The effective mass of a charge carrier is a crucial physical quantity affecting charge and TE transport. Herein, the hole effective masses for these two-dimensional COFs are extracted (Table S4†). It is proven that the hole effective masses of **1–3**, and **5–11** are relatively small ($0.397–0.706m_e$) (Table S4†), comparable with those ($0.20m_e$ and $0.74m_e$)[16] for COF, poly(-tetrathienoanthracene), suggesting their decent charge transport properties. For the other systems, their hole effective masses fall in the range of $1.26–7.10m_e$ (Table S4†).

To shed light on the underlying correlation between the electronic structures and building blocks of COFs, the contributions of knot and linker parts to the valence band are quantified (Fig. 3 and Table S3†). Fig. 3 demonstrates that for our studied two-dimensional COFs, as the ratio of contributions of linker and knot parts to the valence band increases, the valence band widths tend to decrease. Such a phenomenon reveals that the equivalent contribution of knot and linker parts to the valence band is beneficial for hole delocalization and thus large band dispersion.

We identify that for **4**, **10**, and **12–13** with the linker parts of one six-membered ring, the contributions of the linker parts to the valence bands are relatively large, that is, 84.3%, 70.5%, 75.0%, and 80.2%, respectively (Fig. 3 and Table S3†). Furthermore, by comparing **4** and **5**, **10** and **11**, respectively, we find that the contributions of linker parts to the valence band are 84.3%, 54.3%, 70.5%, and 50.0%, respectively (Fig. 3 and Table S3†), proving that introducing benzene rings reduces the contributions of the linker parts to the valence band. Comparing **3** and **16**, **5** and **17**, the contributions to the valence band are 53.0% and 64.0%, 54.3% and 64.5%, respectively, and it is observed that the replacement of the heterocycles with the benzene rings declines the contributions of linker parts to the valence band (Fig. 3 and Table S3†). Thus, we conclude that

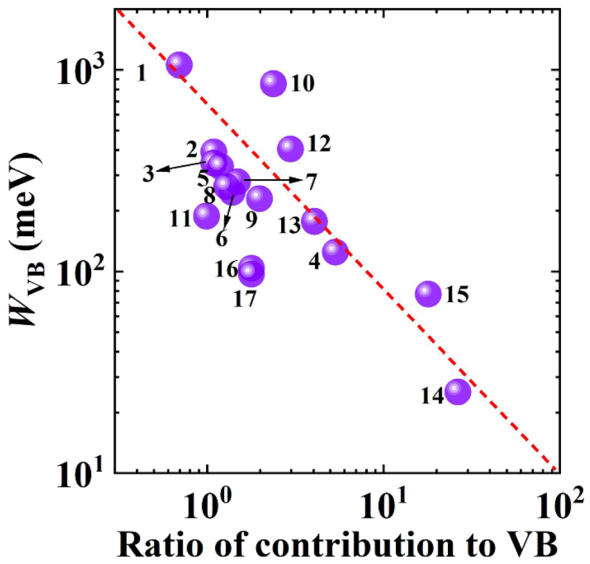

Fig. 3 Relationship between the valence bandwidth (W_{VB}) and ratio of the contributions of the linker parts to the valence bands and the contributions of the knot parts to the valence bands for our studied 17 two-dimensional COFs. The red dashed line displays the trend.

both introducing benzene rings and replacing heterocycles with benzene rings lead to decreased contributions of linker parts to the valence band.

For **6** and **14**, **7** and **15**, it is found that the contributions of their linker parts to the valence bands are 59.0%, 96.4%, 59.8%, and 94.8%, respectively (Fig. 3 and Table S3†), which reveals that the presence of benzoquinone structures elevate the contributions of the linker parts to the valence band, resulting in a relatively flat valence band. Accordingly, we speculate that it is hard for the COFs with linker units of benzoquinone structures to show outstanding charge transport.

Moreover, it is shown that for **3**, and **5–9** with the linker parts of three six-membered rings containing nitrogen heterocycles, the contributions of the linker parts to the valence bands are moderate, namely 53.0%, 54.3%, 59.0%, 59.8%, 56.9%, and 66.4%, respectively (Fig. 3 and Table S3†) and the valence band widths fall in the range of 228–343 meV. Comparing **3** and **6–7**, **5** and **9**, respectively, we demonstrate that increasing the number of nitrogen heterocycles gives rise to enhanced contributions of linker parts to the valence band (Fig. 3 and Table S3†). For **8** and **9**, it is noted that the presence of 1,4-dihydropyrazine reduces the contributions of linker units to the valence band (Fig. 3 and Table S3†). Comparing the contributions of the nitrogen element to the valence bands for **3** and **6–7**, **5** and **9** (*i.e.*, 15.6%, 25.4% and 23.1%, 21.0%, and 32.8%, respectively), respectively (Fig. S7 and Table S5†), we uncover that the large contributions of the nitrogen element to the valence band lead to the large contributions of the linker part to the valence band.

Furthermore, we prove that the energy-level difference between the highest occupied molecular orbital (HOMO) of the isolated linker and knot parts controls the energy level of the valence band maximum for our studied two-dimensional COFs (Table S6 and Fig. S8†). Specifically, as the energy-level difference between the HOMO of the isolated linker and knot parts increases, the valence band maximum of COF is raised (Fig. S8†), indicating that it is easier for charge to transfer from the host COF to the additional dopant, and thereby to achieve p-type chemical doping. This finding hints that the doping efficiency of COF-based materials can be effectively tuned through engineering their building blocks.

Quantitative descriptions of the interaction of charge carriers with lattice vibrations

The coupling between the motions of the charge carriers and lattice vibrations (*i.e.*, electron–phonon coupling) is a critical microscopic process determining charge and TE transport.[46] Previous theoretical explorations have proven that the electron scattering process in two-dimensional single-layer carbon-based materials is primarily governed by a low-frequency acoustic phonon near room temperature.[47–49] Hence, acoustic phonon scatterings are herein taken into account by employing the DP theory.[30] In this theory, the DP constant and elastic constant are two key parameters quantifying the strength of coupling between the electron and acoustic phonon.[50,51] The detailed first-principles computational methods for these two parameters can be found in the Method section and Section 1 of the ESI.†

Our calculated DP constants for these 17 two-dimensional COFs fall in the range of 1.59–3.67 eV (Table S7†). For **1**, **8**, **11**, and **13**, their DP constants are about 3.14–3.67 eV (Table S7†), comparable with the previously theoretically reported ones for graphene-like materials, such as graphyne and its derivatives (2.91–3.56 eV).[52] Our evaluated elastic constants fall in the range of 100–330 J m^{-2} (Table S7†), close to the previously calculated ones for graphene and its derivatives (90–330 J m^{-2}),[52] apparently evidencing the rigid skeleton structures of two-dimensional COFs.

The relaxation time (also known as scattering time) describes how quickly the charge carrier recovers from a non-equilibrium state to an equilibrium state *via* lattice vibrations, which is a critical parameter quantifying the strength of electron–phonon coupling.[46] We find that for our studied systems, the evaluated room-temperature hole relaxation times increase with increased valence band dispersion (Fig. 4a). Such a phenomenon can be attributed to that a large bandwidth brings about a small probability that the charge carrier with a certain energy is scattered to another state with similar energy, thus resulting in a long relaxation time.

It is demonstrated that for our studied COFs, their hole relaxation times fall in the range of 2.95–836 fs at room temperature (Fig. 4a and Table S8†). Specifically, the hole relaxation times of **1–2**, **13**, **14**, and **16–17** are 95.5, 48.9, 48.6, 29.5, 53.5, and 42.8 fs (Table S8†), respectively, which are comparable with the experimental results for dibenzo[*hi*,*st*]ovalene-COF thin films (~36 fs),[53] crystalline 2D sp^2-carbon frameworks (~41 fs),[54] and two-dimensional COF thin films condensed by 1,3,5-tris(4-aminophenyl)benzene and 1,3,5-triformylbenzene (~70 fs) measured by optical-pump terahertz-probe spectroscopy.[55] Additionally, the hole relaxation times

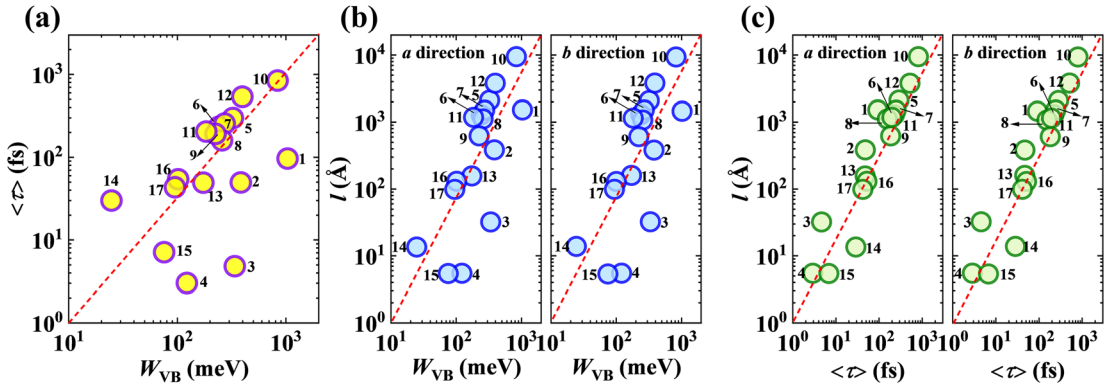

Fig. 4 (a) Relationship between the room-temperature hole relaxation time ($\langle\tau\rangle$) and valence band widths (W_{VB}) for our studied two-dimensional COFs. The red dashed line displays the trend. (b) Relationship between the room-temperature hole mean free path (l) and valence band widths (W_{VB}) along the crystal axis a and b directions. The red dashed lines display the trend. (c) Relationship between the room-temperature hole mean free path (l) and hole relaxation time ($\langle\tau\rangle$) along the crystal axis a and b directions. The red dashed lines display the trend. The detailed data for the calculated room-temperature hole relaxation time and hole mean free path are given in Table S8.†

of **5–12** are in the range of 159–836 fs (Table S8†), lower than the computed results for graphene-like materials (10^3 to 2×10^4 fs).[52]

Fig. 4b displays the relationship between the computed hole mean free path and valence band dispersion for our studied COFs. Importantly, it can be seen that the room-temperature hole mean free path increases as the valence band dispersion enlarges. The *a*- and *b*-axis hole mean free paths for these COFs are almost equal (Fig. 4b and Table S8†), implying the isotropic charge transport behavior. Besides, it is found that the calculated hole mean free path of our studied COFs varies widely ($\sim 10^0$ to 10^4 Å) (Fig. 4b and Table S8†). For instance, **10** exhibits the longest hole mean free path of 9.42×10^3 Å, while **15** exhibits the shortest one of 5.29 Å (Fig. 4b and Table S8†). The hole mean free paths of **1–2**, **5–13**, and **16** fall in the range of 10^2 to 10^4 Å (Fig. 4b and Table S8†), comparable with those for monolayer graphene ($\sim$230 Å)[56] measured using the terahertz-cavity-enhanced-optical Hall effect and graphene ($\sim 10^3$ Å)[57] calculated from first principles. Moreover, the hole mean free paths of **3–4**, **14–15**, and **17** (10^0 to 10^2 Å) (Fig. 4b and Table S8†) are close to the computed intrachain mean free path for conducting polymers, such as poly(3,4-ethylenedioxythiophene) (13.2 Å)[43] and poly(3-hexylthiophene) (48 Å).[44]

Fig. 4c shows that for our studied materials, the computed room-temperature hole mean free path increases as the relaxation time increases. Such a phenomenon reveals that the increase in valence band dispersion plays a dominant role in the elevation of the hole mean free path for these systems, which clearly highlights that engineering electronic structures for two-dimensional COFs holds the key to refining their charge transport.

First-principles predictions of TE transport properties

Intrinsic charge carrier mobility (μ), a key macroscopic physical quantity, controls the TE properties of a material through the relation, $\sigma = Ne\mu$, in which σ is the conductivity; N is the charge carrier concentration, and e is the elementary charge. Fig. 5a and b show that for our studied two-dimensional COFs, the computed room-temperature hole mobility enhances with the increased hole mean free path, suggesting that the electron–phonon interactions play a dominant role in their charge transport process.

It is proven that for our studied systems, their calculated hole mobilities exhibit isotropic characteristics (Fig. 5a, b and Table S8†), in line with the above-mentioned hole mean free path. Among these 17 materials, **5** possesses a large hole mean free path (2.10×10^3 and 2.08×10^3 Å for the *a* and *b* directions, respectively) (Table S8†) and the highest hole mobility (5.35×10^3 and 4.92×10^3 cm^2 V^{-1} s^{-1} along the *a* and *b* directions, respectively) (Fig. 5a, b and Table S8†), which stem from its small ratio of contributions of linker and knot parts to the valence band and its moderate valence band dispersion (Fig. 3). **4** shows the shortest hole mean free path (5.33 and 5.35 Å for the *a* and *b* directions, respectively) and the lowest hole mobility (0.502 and 0.502 cm^2 V^{-1} s^{-1} for the *a* and *b* directions, respectively) (Fig. 5a, b and Table S8†), due to its large ratio of contributions of linker and knot units to the valence band and its flat valence band dispersion (Fig. 3). The evaluated hole mobilities of **1–2**, **7**, and **10** are around 1.2×10^3 to 3.2×10^3 cm^2 V^{-1} s^{-1}, lower than that of **5**, but much higher than those for the other COFs ($\sim 10^{-1}$ to 694 cm^2 V^{-1} s^{-1}) (Fig. 5a, b and Table S8†). Overall, for our studied two-dimensional COFs, their calculated hole mobilities fall in the range of 10^{-1} to 10^4 cm^2 V^{-1} s^{-1} (Fig. 5a, b and Table S8†), comparable with those for the currently advanced two-dimensional COFs (1 to 10^3 cm^2 V^{-1} s^{-1})[18,38–40,58] (Fig. 6a and Table S11†).

Previous experimental studies have demonstrated that the charge carrier concentrations of some representative COFs can reach the range of 5×10^{11} to 5×10^{18} cm^{-3} (Table S9†). Therefore, in the following, the TE properties of our studied COFs at a hole concentration of 5×10^{13} to 10^{15} cm^{-3} are discussed. On the basis of the rigid band approximation, we regulate the hole concentration to optimize the TE transport coefficients, including the Seebeck coefficient, conductivity,

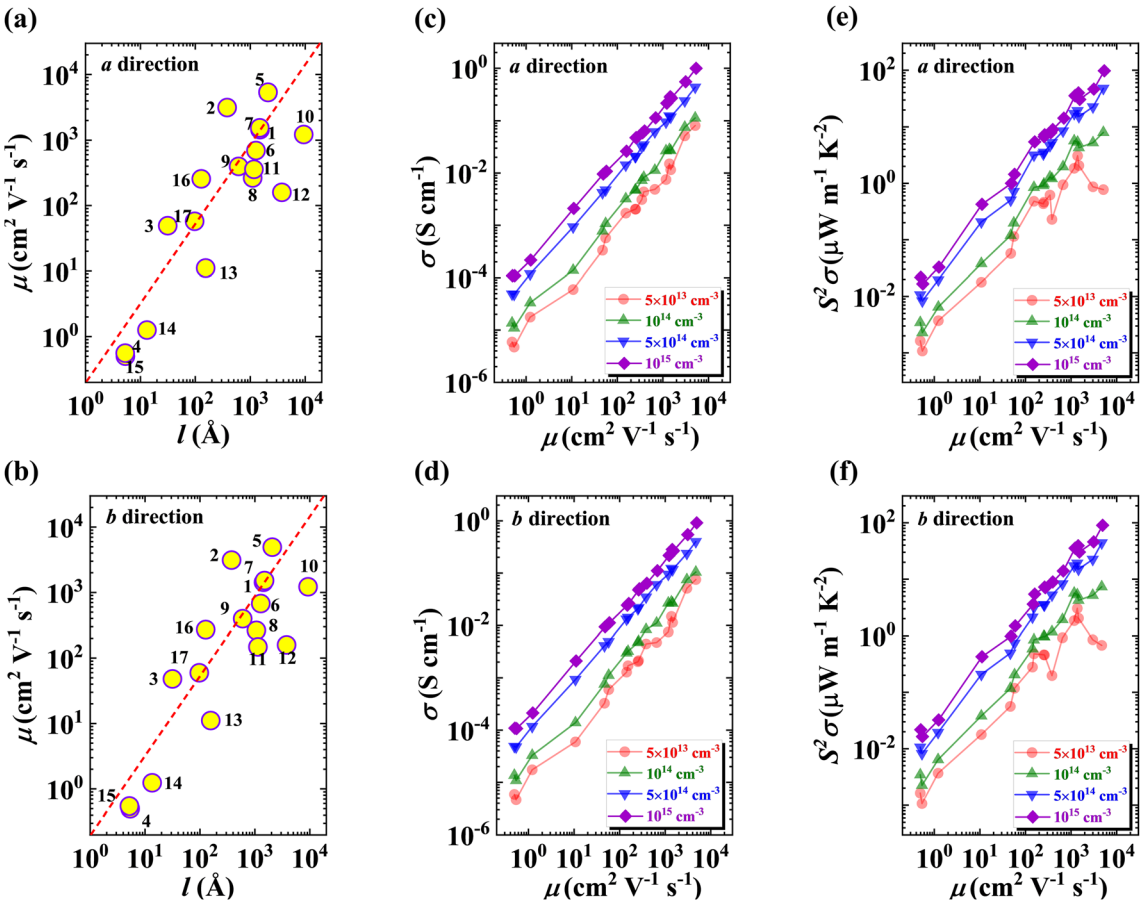

Fig. 5 Dependence of room-temperature hole mobility (μ) on the hole mean free path (l) along the (a) *a* and (b) *b* directions, respectively for our studied two-dimensional COFs. Relationship between the room-temperature conductivity (σ) at different hole concentrations and hole mobility (μ) along the (c) *a* and (d) *b* directions, respectively. Relationship between the room-temperature TE power factor ($S^2\sigma$) at different hole concentrations and hole mobility (μ) along the (e) *a* and (f) *b* directions, respectively.

and power factor by shifting the Fermi energy level (Fig. S9†).[59] It is found that for our studied COFs, as the hole concentration increases, their Seebeck coefficient dramatically declines, while their conductivity and power factor increase (Fig. S9†).

Fig. 5c and d exhibit that for our studied materials, their *a*- and *b*-axis hole conductivities show obviously isotropic features owing to their isotropic mobilities. Furthermore, it is demonstrated that the hole conductivities at the same concentration of these 17 COFs vary greatly (Fig. 5c, d and Table S10†). For example, their conductivities fall in the range of 1.09×10^{-4} to 10^{0} S cm^{-1} at a carrier concentration of 10^{15} cm^{-3} (Fig. 5c, d and Table S10†), which originates from their quite different hole mobilities (Fig. 5a, b and Table S8†).

As a result of its small ratio of contributions of linker and knot parts to the valence band, moderate valence band dispersion, and weak electron–phonon interactions, **5** exhibits the largest room-temperature *a*-axis hole conductivities of 0.0797, 0.112, 0.429, and 0.995 S cm^{-1} and *b*-axis ones of 0.0737, 0.103, 0.394, and 0.915 S cm^{-1} at the concentrations of 5×10^{13}, 10^{14}, 5×10^{14}, and 10^{15} cm^{-3}, respectively (Fig. 5c, d and Table S10†). **15** possess large ratios of contributions of linker and knot parts to the valence band, relatively flat valence band dispersion, and strong electron–phonon interactions, which leads to their lowest room-temperature hole mobilities, and *a*-axis hole conductivities of 4.52×10^{-6}, 1.05×10^{-5}, 4.65×10^{-5}, and 1.09×10^{-4} S cm^{-1} and *b*-axis ones of 4.44×10^{-6}, 1.04×10^{-5}, 4.57×10^{-5}, and 1.07×10^{-4} S cm^{-1} at the concentrations of 5×10^{13}, 10^{14}, 5×10^{14}, and 10^{15} cm^{-3}, respectively (Fig. 5c, d and Table S10†). Furthermore, the experimental investigations have demonstrated that the measured conductivities of some state-of-the-art COFs fall in the range of 10^{-6} to 10^{-2} S cm^{-1} at room temperature, close to our predicted ones ($\sim 10^{-6}$ to 10^{0} S cm^{-1}) (Fig. 6c and Table S11†), which suggests the rationality of our calculated results.

Our computed Seebeck coefficients at the same carrier concentration are mostly close (Fig. 6b and Table S10†). In experiments, the measured room-temperature Seebeck coefficients of the compressed pellets of fluorene-based COF are 1700–3300 μV K^{-1} at different iodine doping levels,[17] and our calculated ones are in the range of 300–1734 μV K^{-1} within the range of carrier concentration studied (Table S10†). Therefore, our predicted Seebeck coefficients for these COFs are in the same order of magnitude as the experimental measurements (Fig. 6b).

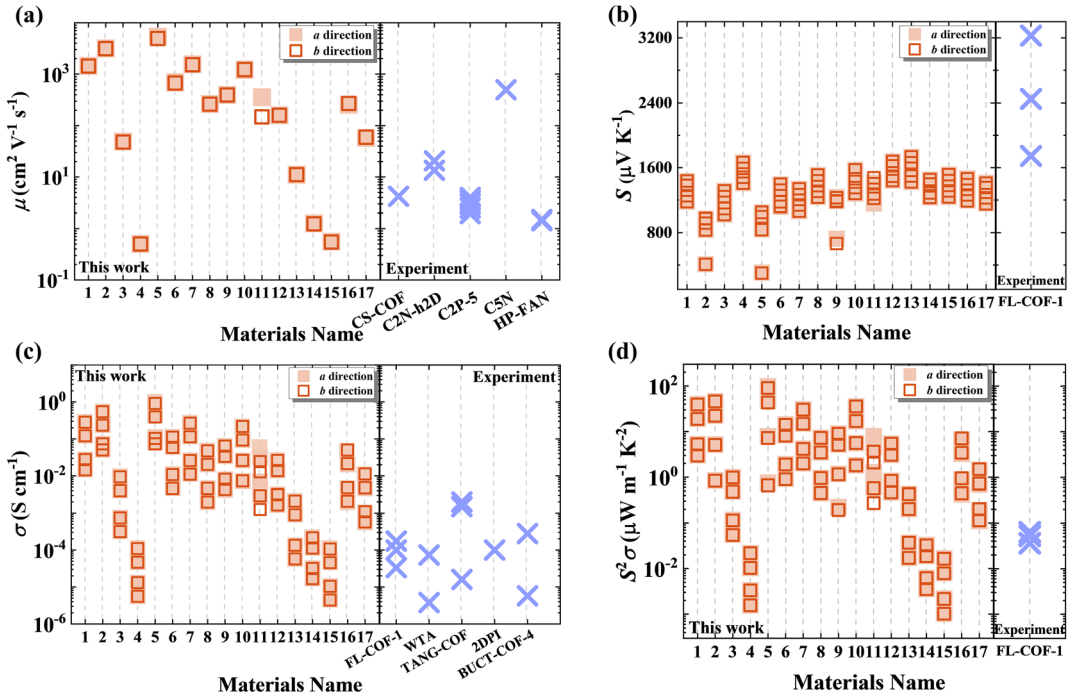

Fig. 6 Comparison of the calculated results of the 17 two-dimensional COFs (square) and the measured results of some advanced COFs (cross) for (a) hole mobilities (μ), (b) Seebeck coefficients (S), (c) conductivities (σ), and (d) TE power factors ($S^2\sigma$) at room temperature.

For our studied two-dimensional COFs, their power factors increase along with the enhanced hole mobilities (Fig. 5e and f). The computed *a*- and *b*-axis power factors are almost equal (Fig. 5e, f and Table S10†), showing isotropic characteristic. At a hole concentration of 10^{15} cm^{-3}, the calculated room-temperature power factors of these two-dimensional COFs fall in the range of 10^{-2} to 10^{2} μW m^{-1} K^{-2} (Fig. 5e, f and Table S10†). Among our studied COFs, due to their excellent mobility (5.35×10^3 and 4.92×10^3 cm^2 V^{-1} s^{-1} along the *a* and *b* directions, respectively) (Fig. 5a, b and Table S8†), **5** exhibits the best room-temperature power factor (97.8 and 90.3 μW m^{-1} K^{-2} along the *a* and *b* directions, respectively) at a hole concentration of 10^{15} cm^{-3} (Fig. 5e, f and Table S10†), approximately four orders of magnitude higher than those for **4** and **14–15** (0.0217, 0.0328, and 0.0167 μW m^{-1} K^{-2} along the *a* direction and 0.0217, 0.323, and 0.0164 μW m^{-1} K^{-2} along the *b* direction, respectively) (Fig. 5e, f and Table S10†).

Compared with **5** which has the linker part of one pyrazine ring, the linker part of **9** possesses two pyrazine rings. Although they have analogous structures, their electronic structures are quite different (Fig. 2e and i). **5** exhibits a smaller ratio of the contributions of linker and knot parts to the valence band than **9** (Fig. 3). Therefore, **5** shows a larger band dispersion (*i.e.*, a more delocalized charge carrier feature), weaker electron–phonon interactions, higher hole mobility, and thereby a larger power factor (Fig. 5, and Table S10†).

13 possesses a large ratio of contributions from linker and knot parts to the valence band. Consequently, it displays a relatively flat valence band dispersion, short hole relaxation time, low mobility, and thus a low power factor of 0.0172–0.426 μW m^{-1} K^{-2} at a hole concentration of 5×10^{13} to 1×10^{15} cm^{-3} (Fig. 5, 6 and Table S10†). Compared with **13**, **12** exhibits a smaller ratio of contributions of linker and knot parts to the valence band (Fig. 3). Hence, it shows a moderate valence band dispersion, longer hole relaxation time, higher mobility, and thereby a larger power factor of 0.468–5.42 μW m^{-1} K^{-2} at a hole concentration of 5×10^{13} to 1×10^{15} cm^{-3} (Fig. 5, and Table S10†).

Moreover, the relationship between the TE properties and pore diameter for our studied two-dimensional COFs is explored. Interestingly, no significant correlations between the Seebeck coefficient, conductivity, power factor, mobility, and pore diameter are observed for our studied systems (Fig. S10, Table S12, and Fig. S11†).

The effect of different functional groups and moieties on the TE properties

To the best of our knowledge, few experimental studies have systematically explored how different functional groups and moieties impact the TE properties of COFs so far. Consequently, to probe such an effect, we further carefully analyze our current computed results. For instance, it is demonstrated that for **2** and **5**, replacement of the benzene ring with a pyrazine ring in the linker parts has a small effect on the power factor (0.834–46.2 μW m^{-1} K^{-2} for **2** and 0.664–97.8 μW m^{-1} K^{-2} for **5** at a hole concentration of 5×10^{13} to 1×10^{15} cm^{-3}) (Fig. 7a and Table S10†), owing to their similar valence band dispersions (390 and 330 meV for **2** and **5**, respectively) (Fig. 2 and Table S3†). In contrast, we reveal that for **4** and **10**, replacement of

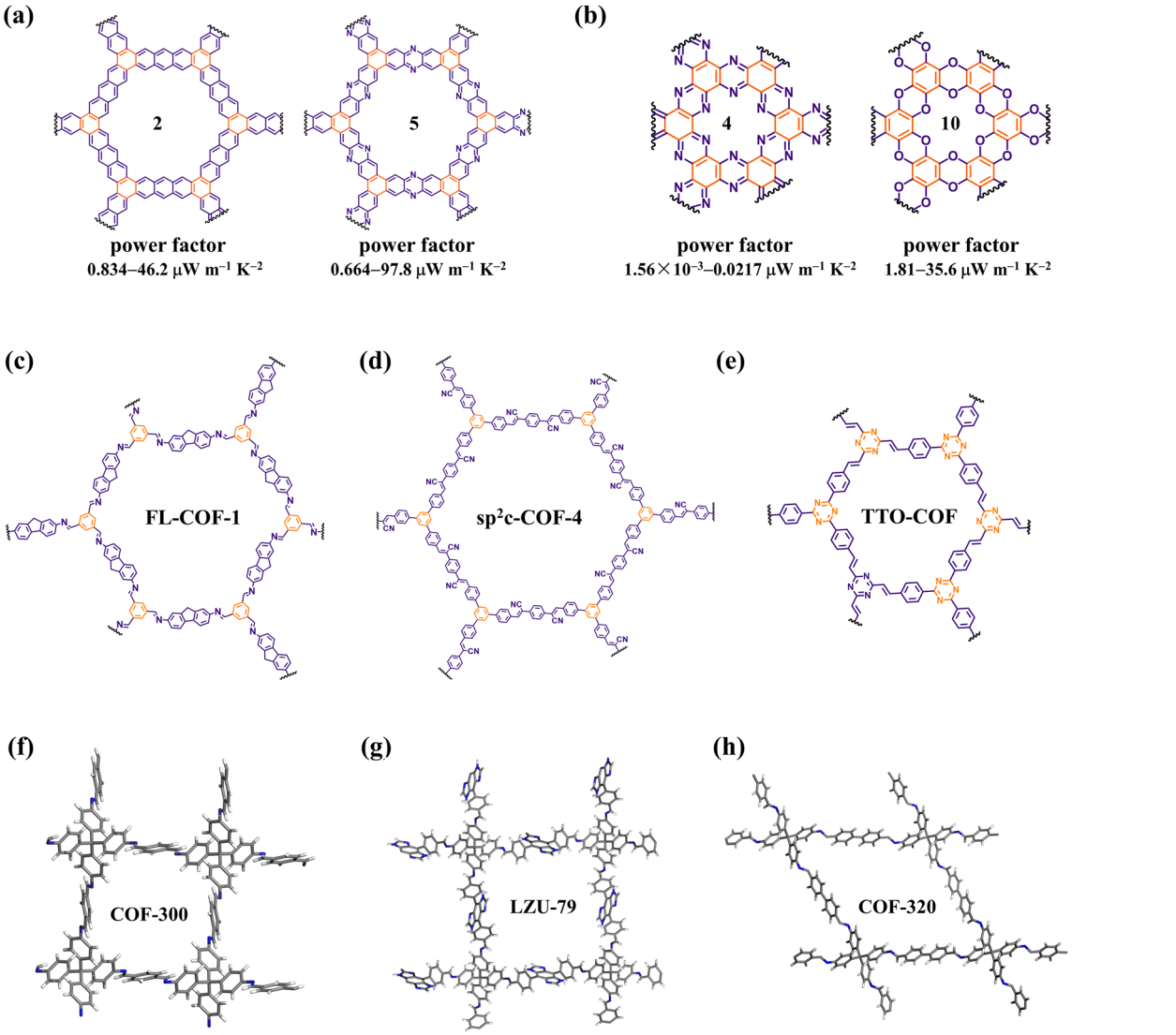

Fig. 7 Chemical structures of (a) **2** and **5** and (b) **4** and **10**. Their calculated room-temperature power factors at a hole concentration of 5×10^{13} to 1×10^{15} cm^{-3} are displayed in the figure. Chemical structures of (c) **FL-COF-1**, (d) **sp²c-COF-4**, and (e) **TTO-COF**. The linker and knot parts are displayed in purple and orange, respectively. The crystal structures of (f) **COF-300**, (g) **LZU-79**, and (h) **COF-320**. The carbon and nitrogen atoms are represented in grey and blue, respectively.

pyrazine with a 1,4-dioxin ring in the linker parts results in a remarkable enhancement of the power factor (1.56×10^{-3} to 0.0217 μW m^{-1} K^{-2} for **4** and 1.81–35.6 μW m^{-1} K^{-2} for **10** at a hole concentration of 5×10^{13} to 1×10^{15} cm^{-3}) (Fig. 7b and Table S10†), because **10** exhibits much larger valence band dispersion (852 meV) than **4** (124 meV) (Fig. 2 and Table S3†).

Recently, it has been theoretically demonstrated that thiophene ring orientations in two-dimensional COFs have a significant influence on their TE properties.[16] Researchers uncover that a typical two-dimensional COF, poly(tetrathienoanthracene), possesses higher p-type room-temperature Seebeck coefficients (~90–570 μV K^{-1}) than its isomer (~20–380 μV K^{-1}) with α-linked thiophene rings along the *ortho* direction at a hole concentration of $\sim 5 \times 10^{18}$ to 1×10^{21} cm^{-3}, due to the coexistence of a large dispersive valence band and sharp peak of density of states near the band edge for the former.[16]

Implications for other classes of COFs

Recently, lots of fascinating experimental advances on COFs with diverse geometric structures have been reported.[10,12] We select a fluorine-based two-dimensional COF (**FL-COF-1**) that has been experimentally demonstrated for TE applications[17] (Fig. 7c), to compute its p-type TE properties. It is revealed that its calculated Seebeck coefficients fall in the range of 1.25×10^3 to 1.52×10^3 μV K^{-1}; its conductivities are in the range of 1.54×10^{-4} to 3.75×10^{-3} S cm^{-1}; and its power factors fall in the range of 0.0355–0.582 μW m^{-1} K^{-2} at a hole concentration of 5×10^{13} to 1×10^{15} cm^{-3} (Table S13†), comparable with the measured results (1.75×10^3 to 3.23×10^3 μV K^{-1} for Seebeck coefficients, 3.34×10^{-5} to 1.75×10^{-4} S cm^{-1} for conductivities, and 0.0362–0.063 μW m^{-1} K^{-2} for power factors) (Fig. S13†), which corroborates the generality of our used computational method.

A typical C=C linked sp^2c-COF (*i.e.*, hexagonal **sp^2c-COF-4**)[60] (Fig. 7d) is selected to calculate its band structure. It is demonstrated that **sp^2c-COF-4** exhibits a valence band dispersion of 8.22 meV (Fig. S14†), larger than that (0.174 meV) for the fluorine-based COF (Fig. S12†), which indicates a more delocalized charge carrier feature, possibly higher mobility, and a larger power factor for **sp^2c-COF-4**.

Besides, we also explore the TE properties of a typical two-dimensional COF with a triazine core (*i.e.*, **TTO-COF**)[61] (Fig. 7e). We find that for this COF, its calculated power factors fall in the range of 1.80×10^{-5} to 4.60×10^{-4} $\mu W\ m^{-1}\ K^{-2}$ at a hole concentration of 5×10^{13} to 1×10^{15} cm^{-3} (Fig. S16 and Table S14†). It is worth noting that the predicted power factors of our studied 17 two-dimensional COFs with the core part of benzene rings fall in the range of 1.02×10^{-3} to 97.8 $\mu W\ m^{-1}\ K^{-2}$ (Fig. 6 and Table S10†), higher than those for **TTO-COF** with a triazine core.

Researchers have found that in addition to two-dimensional TE materials, by employing popular nanostructuring strategies, the TE performance of three-dimensional TE materials can be significantly elevated, due to energy filtering induced Seebeck coefficient improvement and phonon scattering caused thermal conductivity attenuation.[42] Inspired by this progress, three representative experimentally prepared single-crystal three-dimensional COFs (*i.e.*, **COF-300**,[62] **LZU-79**,[62] and **COF-320** (ref. 63)) (Fig. 7f–h) are utilized to examine their band structures. We demonstrate that they exhibit moderate valence band dispersions (195, 180, and 200 meV for **COF-300**, **LZU-79**, and **COF-320**, respectively) (Fig. S17†), indicating their potential heat-electricity interconversion applications.

Conclusions

In summary, on the basis of comprehensive *ab initio* investigations, we establish an atomistic-level framework to unveil the underlying correlation among the macroscopic TE power factor, nontrivial transport processes, and fundamental chemical structures for emerging two-dimensional COF materials. We reveal that the ratio of contributions of linker and knot parts to the valence bands is a strong predictor to assess the TE performance of COFs. Specifically, a small ratio of the contributions of linker and knot parts to the valence bands gives rise to a large band dispersion (*i.e.*, a delocalized charge carrier feature), weak electron–phonon interactions, high hole mobility, and thereby superb power factors. Furthermore, on the basis of this materials design strategy, our computational results uncover that for two-dimensional COFs, introducing benzene rings, replacing the heterocycles with benzene rings, reducing the number of nitrogen heterocycles, and avoiding the benzoquinone structures in the linker parts help in achieving their hole delocalization, and thus decent power factors. We anticipate that our proposed new atomistic design principles will rationalize the TE response properties of the two-dimensional COF family and facilitate the systematic development of new materials with enhanced performance.

Author contributions

W. S. conceived and designed this study. T. X. Z. performed the electronic structure calculations and computed the electron–phonon interactions, relaxation times, and thermoelectric transport coefficients. X. M. W. contributed to the calculations of thermoelectric transport coefficients and the interpretation of their data. H. Y. L. contributed to the interpretation of the data. T. Q. D. and Z. B. G. contributed to the electron–phonon interaction calculations and the interpretation of their data. T. X. Z. prepared the figures and tables. T. X. Z. and W. S. wrote the manuscript with discussion and input from all authors.

Conflicts of interest

There are no competing interests.

Acknowledgements

This work was supported by the National Natural Science Foundation of China (Grant No. 3100041031094, No. 12104356, and No. 52250191), the Guangdong Natural Science Foundation (Grant No. 3100042030822), the Guangzhou Science and Technology Plan Project (Grant No. 3100042051068), the Fundamental Research Funds for the Central Universities, Sun Yat-sen University (Grant No. 3100031610843), and the 100 Talents Plan Foundation of Sun Yat-sen University (Grant No. 3100012220013). Computational resources were provided by the National Supercomputer Center in Guangzhou.

References

1 J. He and T. M. Tritt, *Science*, 2017, **357**, 1369.
2 F. J. DiSalvo, *Science*, 1999, **285**, 703–706.
3 L. E. Bell, *Science*, 2008, **321**, 1457–1461.
4 G. J. Snyder and E. S. Toberer, *Nat. Mater.*, 2008, **7**, 105–114.
5 B. Russ, A. Glaudell, J. J. Urban, M. L. Chabinyc and R. A. Segalman, *Nat. Rev. Mater.*, 2016, **1**, 16050.
6 M. Massetti, F. Jiao, A. J. Ferguson, D. Zhao, K. Wijeratne, A. Wurger, J. L. Blackburn, X. Crispin and S. Fabiano, *Chem. Rev.*, 2021, **121**, 12465–12547.
7 G. H. Kim, L. Shao, K. Zhang and K. P. Pipe, *Nat. Mater.*, 2013, **12**, 719–723.
8 T. Park, C. Park, B. Kim, H. Shin and E. Kim, *Energy Environ. Sci.*, 2013, **6**, 788–791.
9 O. Bubnova, Z. U. Khan, A. Malti, S. Braun, M. Fahlman, M. Berggren and X. Crispin, *Nat. Mater.*, 2011, **10**, 429–433.
10 C. S. Diercks and O. M. Yaghi, *Science*, 2017, **355**, eaal1585.
11 N. Huang, P. Wang and D. Jiang, *Nat. Rev. Mater.*, 2016, **1**, 16068.
12 K. Geng, T. He, R. Liu, S. Dalapati, K. T. Tan, Z. Li, S. Tao, Y. Gong, Q. Jiang and D. Jiang, *Chem. Rev.*, 2020, **120**, 8814–8933.
13 H. Zhang, Y. Geng, J. Huang, Z. Wang, K. Du and H. Li, *Energy Environ. Sci.*, 2023, **16**, 889–951.
14 S. Yang, D. Streater, C. Fiankor, J. Zhang and J. Huang, *J. Am. Chem. Soc.*, 2021, **143**, 1061–1068.

15 A. C. Jakowetz, T. F. Hinrichsen, L. Ascherl, T. Sick, M. Calik, F. Auras, D. D. Medina, R. H. Friend, A. Rao and T. Bein, *J. Am. Chem. Soc.*, 2019, **141**, 11565–11571.
16 T. Deng, X. Yong, W. Shi, Z. M. Wong, G. Wu, H. Pan, J.-S. Wang and S.-W. Yang, *J. Mater. Chem. A*, 2020, **8**, 4257–4262.
17 L. Wang, B. Dong, R. Ge, F. Jiang and J. Xu, *ACS Appl. Mater. Interfaces*, 2017, **9**, 7108–7114.
18 J. Mahmood, E. K. Lee, H. J. Noh, I. Ahmad, J. M. Seo, Y. K. Im, J. P. Jeon, S. J. Kim, J. H. Oh and J. B. Baek, *Adv. Mater.*, 2021, **33**, e2004707.
19 A. Giri and P. E. Hopkins, *Nano Lett.*, 2021, **21**, 6188–6193.
20 P. E. Blochl, *Phys. Rev. B: Condens. Matter Mater. Phys.*, 1994, **50**, 17953–17979.
21 J. P. Perdew, K. Burke and M. Ernzerhof, *Phys. Rev. Lett.*, 1996, **77**, 3865–3868.
22 S. Grimme, J. Antony, S. Ehrlich and H. Krieg, *J. Chem. Phys.*, 2010, **132**, 154104.
23 G. Kresse and J. Furthmüller, *Comput. Mater. Sci.*, 1996, **6**, 15–50.
24 L.-F. Huang, B. Grabowski, E. McEniry, D. R. Trinkle and J. Neugebauer, *Phys. Status Solidi B*, 2015, **252**, 1907–1924.
25 C. Lee, W. Yang and R. G. Parr, *Phys. Rev. B: Condens. Matter Mater. Phys.*, 1988, **37**, 785–789.
26 G. W. T. M. J. Frisch, H. B. Schlegel, G. E. Scuseria, J. R. C. M. A. Robb, G. Scalmani, V. Barone, B. Mennucci, H. N. G. A. Petersson, M. Caricato, X. Li, H. P. Hratchian, J. B. A. F. Izmaylov, G. Zheng, J. L. Sonnenberg, M. Hada, K. T. M. Ehara, R. Fukuda, J. Hasegawa, M. Ishida, T. Nakajima, O. K. Y. Honda, H. Nakai, T. Vreven, J. A. Montgomery Jr, F. O. J. E. Peralta, M. Bearpark, J. J. Heyd, E. Brothers, V. N. S. K. N. Kudin, R. Kobayashi, J. Normand, A. R. K. Raghavachari, J. C. Burant, S. S. Iyengar, J. Tomasi, N. R. M. Cossi, J. M. Millam, M. Klene, J. E. Knox, J. B. Cross, C. A. V. Bakken, J. Jaramillo, R. Gomperts, R. E. Stratmann, A. J. A. O. Yazyev, R. Cammi, C. Pomelli, J. W. Ochterski, K. M. R. L. Martin, V. G. Zakrzewski, G. A. Voth, J. J. D. P. Salvador, S. Dapprich, A. D. Daniels, J. B. F. O. Farkas, J. V. Ortiz, J. Cioslowski and D. J. Fox, *Gaussian 09*, Gaussian, Inc., Wallingford CT, 2009.
27 D. Wang, W. Shi, J. Chen, J. Xi and Z. Shuai, *Phys. Chem. Chem. Phys.*, 2012, **14**, 16505–16520.
28 W. Shi, J. Chen, J. Xi, D. Wang and Z. Shuai, *Chem. Mater.*, 2014, **26**, 2669–2677.
29 G. K. Madsen, *J. Am. Chem. Soc.*, 2006, **128**, 12140–12146.
30 J. Bardeen and W. Shockley, *Phys. Rev.*, 1950, **80**, 72–80.
31 W. Shi, T. Zhao, J. Xi, D. Wang and Z. Shuai, *J. Am. Chem. Soc.*, 2015, **137**, 12929–12938.
32 W. Shi, Z. M. Wong, T. Deng, G. Wu and S. W. Yang, *Adv. Funct. Mater.*, 2020, **31**, 1901956.
33 W. Shi, T. Deng, Z. M. Wong, G. Wu and S.-W. Yang, *npj Comput. Mater.*, 2021, **7**, 107.
34 W. Shi, G. Wu, K. Hippalgaonkar, J. S. Wang, J. Xu and S. W. Yang, *J. Am. Chem. Soc.*, 2018, **140**, 13200–13204.
35 X. Guo, T. Zheng, G. Ji, N. Hu, C. Xu and Y. Zhang, *J. Mater. Chem. A*, 2018, **6**, 10243–10252.
36 W. Shi, G. Wu, X. Yong, T. Deng, J. S. Wang, J. C. Zheng, J. Xu, M. B. Sullivan and S. W. Yang, *ACS Appl. Mater. Interfaces*, 2018, **10**, 35306–35315.
37 X. Guan, H. Li, Y. Ma, M. Xue, Q. Fang, Y. Yan, V. Valtchev and S. Qiu, *Nat. Chem.*, 2019, **11**, 587–594.
38 J. Guo, Y. Xu, S. Jin, L. Chen, T. Kaji, Y. Honsho, M. A. Addicoat, J. Kim, A. Saeki, H. Ihee, S. Seki, S. Irle, M. Hiramoto, J. Gao and D. Jiang, *Nat. Commun.*, 2013, **4**, 2736.
39 S. Jhulki, J. Kim, I.-C. Hwang, G. Haider, J. Park, J. Y. Park, Y. Lee, W. Hwang, A. A. Dar, B. Dhara, S. H. Lee, J. Kim, J. Y. Koo, M. H. Jo, C.-C. Hwang, Y. H. Jung, Y. Park, M. Kataria, Y.-F. Chen, S.-H. Jhi, M.-H. Baik, K. Baek and K. Kim, *Chem*, 2020, **6**, 2035–2045.
40 J. Mahmood, E. K. Lee, M. Jung, D. Shin, I. Y. Jeon, S. M. Jung, H. J. Choi, J. M. Seo, S. Y. Bae, S. D. Sohn, N. Park, J. H. Oh, H. J. Shin and J. B. Baek, *Nat. Commun.*, 2015, **6**, 6486.
41 W. J. Ong and T. M. Swager, *Nat. Chem.*, 2018, **10**, 1023–1030.
42 S. Che and L. Fang, *Chem*, 2020, **6**, 2558–2590.
43 W. Shi, Z. Shuai and D. Wang, *Adv. Funct. Mater.*, 2017, **27**, 1702847.
44 W. Shi, E. Yildirim, G. Wu, Z. M. Wong, T. Deng, J. S. Wang, J. Xu and S. W. Yang, *Adv. Theory Simul.*, 2020, **3**, 2000015.
45 X. Yong, G. Wu, W. Shi, Z. M. Wong, T. Deng, Q. Zhu, X. Yang, J.-S. Wang, J. Xu and S.-W. Yang, *J. Mater. Chem. A*, 2020, **8**, 21852–21861.
46 W. Shi, T. Deng, G. Wu, K. Hippalgaonkar, J. S. Wang and S. W. Yang, *Adv. Mater.*, 2019, **31**, e1901956.
47 Z. Shuai, L. Wang and Q. Li, *Adv. Mater.*, 2011, **23**, 1145–1153.
48 T. Deng, X. Yong, W. Shi, C. K. Gan, W. Li, K. Hippalgaonkar, J. C. Zheng, X. Wang, S. W. Yang, J. S. Wang and G. Wu, *Adv. Electron. Mater.*, 2019, **5**, 2593–2600.
49 M. Long, L. Tang, D. Wang, Y. Li and Z. Shuai, *ACS Nano*, 2011, **5**, 2593–2600.
50 J. Xi, M. Long, L. Tang, D. Wang and Z. Shuai, *Nanoscale*, 2012, **4**, 4348–4369.
51 Z. Shuai, D. Wang, Q. Peng and H. Geng, *Acc. Chem. Res.*, 2014, **47**, 3301–3309.
52 J. Chen, J. Xi, D. Wang and Z. Shuai, *J. Phys. Chem. Lett.*, 2013, **4**, 1443–1448.
53 E. Jin, S. Fu, H. Hanayama, M. A. Addicoat, W. Wei, Q. Chen, R. Graf, K. Landfester, M. Bonn, K. A. I. Zhang, H. I. Wang, K. Mullen and A. Narita, *Angew. Chem., Int. Ed. Engl.*, 2022, **61**, e202114059.
54 E. Jin, M. Asada, Q. Xu, S. Dalapati, M. A. Addicoat, M. A. Brady, H. Xu, T. Nakamura, T. Heine, Q. Chen and D. Jiang, *Science*, 2017, **357**, 673–676.
55 S. Fu, E. Jin, H. Hanayama, W. Zheng, H. Zhang, L. D. Virgilio, M. A. Addicoat, M. Mezger, A. Narita, M. Bonn, K. Mullen and H. I. Wang, *J. Am. Chem. Soc.*, 2022, **144**, 7489–7496.
56 N. Armakavicius, P. Kühne, J. Eriksson, C. Bouhafs, V. Stanishev, I. G. Ivanov, R. Yakimova, A. A. Zakharov, A. Al-Temimy, C. Coletti, M. Schubert and V. Darakchieva, *Carbon*, 2021, **172**, 248–259.

57 T. Y. Kim, C. H. Park and N. Marzari, *Nano Lett.*, 2016, **16**, 2439–2443.
58 H.-J. Noh, S. Chung, M. S. Okyay, Y.-K. Im, S.-W. Kim, D.-H. Kweon, J.-P. Jeon, J.-M. Seo, N.-H. Kim, S.-Y. Yu, Y. Reo, Y.-Y. Noh, B. Kang, N. Park, J. Mahmood, K. Cho and J.-B. Baek, *Chem*, 2022, **8**, 3130–3144.
59 D. Wang, L. Tang, M. Long and Z. Shuai, *J. Chem. Phys.*, 2009, **131**, 224704.
60 E. Jin, K. Geng, K. H. Lee, W. Jiang, J. Li, Q. Jiang, S. Irle and D. Jiang, *Angew. Chem., Int. Ed. Engl.*, 2020, **59**, 12162–12169.
61 Y. Yang, H. Niu, L. Xu, H. Zhang and Y. Cai, *Appl. Catal., B*, 2020, **269**, 118799.
62 T. Ma, E. A. Kapustin, S. X. Yin, L. Liang, Z. Zhou, J. Niu, L. H. Li, Y. Wang, J. Su, J. Li, X. Wang, W. D. Wang, W. Wang, J. Sun and O. M. Yaghi, *Science*, 2018, **361**, 48–52.
63 Y. B. Zhang, J. Su, H. Furukawa, Y. Yun, F. Gandara, A. Duong, X. Zou and O. M. Yaghi, *J. Am. Chem. Soc.*, 2013, **135**, 16336–16339.